Journal of Materials Chemistry C

ROYAL SOCIETY OF CHEMISTRY

PAPER

View Article Online
View Journal | View Issue

Cite this: J. Mater. Chem. C, 2022, 10, 17714

Pressure-sensitive Ce^{3+} photoluminescence in $LiCaY_5(BO_3)_6$: high internal quantum yields and energy transfer to Tb^{3+}†

Yan Gao,[a] Yunwei Zhao,[ab] Pengfei Jiang,[a] Ting Wen,*[b] Yonggang Wang,[c] Rihong Cong *[a] and Tao Yang *[a]

Received 27th August 2022,
Accepted 10th November 2022

DOI: 10.1039/d2tc03611h

rsc.li/materials-c

Ce^{3+} photoluminescence (PL) has attracted attention because spin- and parity-allowed 4f-5d transition ensures brightness, and the susceptibility of the energy level of 5d electrons to the surroundings endow variable emission colors by chemical substitution or physical compression. The PL excitation spectra of $LiCaY_5(BO_3)_6$: xCe^{3+} ($0.01 \leq x \leq 0.15$) exhibit four typical excitation bands covering a wide range from 220 to 380 nm, and $LiCa(Y_{0.99}Ce_{0.01})_5(BO_3)_6$ emits a strong blue light with an internal quantum yield (IQY) of 51%. With an efficient and probably timely energy transfer, co-doping 20% Tb^{3+} leads to an enhancement of the overall IQY to 89%. Blue and green emissions can be obtained by fabricating $LiCa(Y_{0.99}Ce_{0.01})_5(BO_3)_6$ and $LiCa(Y_{0.79}Ce_{0.01}Tb_{0.2})_5(BO_3)_6$ with a 310 nm LED chip, respectively. *In situ* high-temperature photoluminescence spectra for co-doped phosphors exhibit 58% in total emission intensity at 423 K. Most interestingly, the Ce^{3+} PL emission of $LiCa(Y_{0.99}Ce_{0.01})_5(BO_3)_6$ is highly sensitive to applied high pressures, for example, the maximal wavelength of the emission band exhibits a linear red-shift (~43 nm) up to 20.1 GPa, with a susceptibility $d\lambda_{max}/dP$ = 2.05 nm/GPa. Along with the increase in high pressure, the CIE coordinate can be adjusted from (0.195, 0.124) to (0.255, 0.305) under the excitation of 375 nm. These observations suggest its potential application in an optical pressure sensor.

Introduction

White light–emitting diodes (WLEDs) are the predominant technique for solid-state lighting due to the advantages in high brightness, low power consumption, long duration and environmental friendliness.[1–4] The commercialized phosphor converted (pc)-WLEDs to combine the InGaN blue-emitting chip with the highly efficient yellow phosphor $Y_3Al_5O_{12}$:Ce^{3+} (YAG:Ce^{3+}), while the defect lies in the insufficient red component and the resulting high correlated color temperature and low color rendering index.[2,3,5] It is also possible to fabricate the ultraviolet (UV) or near-UV (NUV) LED chip with red, green, and blue phosphors to attain the white light properly.[5,6] Although this may also have the problem in color aberration due to the emission re-absorption or different degradation of phosphors under working conditions, it is an alternative choice and has attracted the attention of researchers.[6] Based on this strategy, great efforts have been made to develop UV or NUV excited phosphors with high efficiency.

Nowadays, the research interest in Ce^{3+}-based phosphors remains high because Ce^{3+} usually exhibits high-brightness and tunable emission (ranging from UV to red in different hosts).[7–9] The ground and excitation configurations are $4f^15d^0$ and $4f^05d^1$, which result in intense absorption and emission bands due to the spin- and parity-allowed 4f-5d transition. In fact, the energy level of the 5d electron is susceptible to the surrounding crystal field,[7] thus the emission color could be tuned by modifying the coordination environment by applying chemical substitution or even physical pressure directly. Moreover, Ce^{3+} is a frequently used sensitizer, transmitting partial excitation energy to co-activators.[10,11] For example, Ce^{3+}-to-Tb^{3+} energy transfer has been reported in $Sr_3Gd_2(BO_3)_4$, $BaLu_2Si_3O_{10}$ and $Ba_2Y_5B_5O_{17}$, where the internal quantum yields (IQYs) are as high as 58%, 71%, and 76%, respectively.[10–12]

In this work, $LiCaY_5(BO_3)_6$: xCe^{3+} ($0.01 \leq x \leq 0.15$) (abbreviated as LCYB: xCe^{3+}) and $LiCaY_5(BO_3)_6$: $0.01Ce^{3+}$, yTb^{3+} ($0.05 \leq y \leq 0.4$) (LCYB: $0.01Ce^{3+}$, yTb^{3+}) were synthesized by

[a] College of Chemistry and Chemical Engineering, Chongqing University, Chongqing 401331, People's Republic of China. E-mail: congrihong@cqu.edu.cn, taoyang@cqu.edu.cn
[b] Center for High Pressure Science and Technology Advanced Research, Beijing 100193, People's Republic of China. E-mail: ting.wen@hpstar.ac.cn
[c] School of Materials Science and Engineering, Peking University, Beijing 100871, People's Republic of China

† Electronic supplementary information (ESI) available: Tables of unit cell lattice parameters, CIE coordinate, fitting parameters to decay curves, IQYs. Figures for the spectral comparison between two singly doped phosphors, and *in situ* high pressure PL emission spectra. See DOI: https://doi.org/10.1039/d2tc03611h

Table 1 Internal quantum yields for Ce^{3+} and Tb^{3+} co-doped phosphors reported in the literature

Host for Ce^{3+} and Tb^{3+} co-doping	Excitation (nm)	IQY	Ref.
$NaBaScSi_2O_7$	349	36%	14
$[Mg_{1.25}Si_{2.5}Al_{2.5}]O_3N_3$	335	41%	15
$Sr_2LiScB_4O_{10}$	365	46%	16
$Sr_4Al_{14}O_{25}$	365	47%	17
$Ca_2GdZr_2Al_3O_{12}$	408	54%	18
$Sr_3Gd_2(BO_3)_4$	345	58%	10
$Sr_2MgB_2O_6$	323	66%	19
$Ca_2LuZr_2(AlO_4)_3$	408	69%	20
$BaLu_2Si_3O_{10}$	365	71%	11
$Ba_2Y_5B_5O_{17}$	345	76%	12
$Ca_2GdHf_2Al_3O_{12}$	408	83%	21
$La_8Ba_2(Si_4P_2O_{22}N_2)O_2$	290	89%	22
$LiCaY_5(BO_3)_6$	336	89%	This work
$Ba_3Y_2B_6O_{15}$	365	93%	23
$Ca_3Gd_2Si_6O_{18}$	325	95%	13

high-temperature solid-state reactions. Color-tunable emissions from blue to green can be realized by increasing the Tb^{3+} content. The energy transfer efficiency increases monotonously on increasing y and achieves 92% at the maximal Tb^{3+}-doping. $LiCa(Y_{0.79}Ce_{0.01}Tb_{0.2})_5(BO_3)_6$ exhibits the highest internal quantum efficiency of 89% when excited at 336 nm. Such a high value of IQY is rarely reported in the literature (see Table 1).[10–23] A trial to combine this optimal phosphor with the 310 nm LED chip leads to green emission, indicating its potential as the LED-pumped green phosphor. Most importantly, *in situ* high-pressure photoluminescence of $LiCa(Y_{0.99}Ce_{0.0.1})_5(BO_3)_6$ up to 20.1 GPa exhibits a high susceptibility of $d\lambda_{max}/dP$ = 2.05 nm/GPa, where λ_{max} is the wavelength at the maximal emission intensity. This value is even higher than that of ruby (Al_2O_3:Cr^{3+}, $d\lambda/dP$ = 0.36 nm/GPa), which is commonly used as the pressure sensor.[24] The Raman spectra at high pressures suggest no phase transition, and this high-pressure susceptibility in the emission is intrinsic for $LiCa(Y_{0.99}Ce_{0.0.1})_5(BO_3)_6$, making it a potential candidate for pressure sensors.

Experimental section

$LiCa(Y_{1-x}Ce_x)_5(BO_3)_6$ ($0.01 \leq x \leq 0.15$) and $LiCa(Y_{0.99-y}Ce_{0.01}Tb_y)_5(BO_3)_6$ ($0.05 \leq y \leq 0.40$) polycrystalline samples were synthesized by traditional high-temperature solid-state reactions. Starting materials include Li_2CO_3 (99%), $CaCO_3$ (99%), Y_2O_3 (99.999%), $Ce(NO_3)_3{\cdot}6H_2O$ (99.9%), Tb_4O_7 (99.99%), and H_3BO_3 (A.R. with 10% excess in order to compensate the volatilization of boron at high temperatures). Appropriate amounts of chemicals were mixed and ground in an agate mortar thoroughly according to the formula. The powder was pressed into a pellet with φ = 13 mm and was placed in an Al_2O_3 boat. The sample was annealed in a tube furnace at 780 °C for 10 h, and a reducing gas (10% H_2 and 90% Ar) is necessary to obtain Ce^{3+}. After naturally cooling down, the pellet was taken out and ground into a white powder for further characterizations.

Phase purity was studied by powder X-ray diffraction (PXRD) using a PANalytical Empyrean powder diffractometer with Cu Kα radiation (1.5406 Å). The scanning range is from 10° to 80° (2θ), and the operating voltage and current are 40 kV and 40 mA, respectively. Le Bail refinements were conducted using the TOPAS software package.[25] Room-temperature PL excitation and emission spectra were measured using a Hitachi F-4600 spectrometer equipped with a 150 W xenon lamp as the excitation source. Both of the input and output slits were 1.0 nm, and the voltage of the photomultiplier tube was 700 V. *In situ* high-temperature PL spectra and internal quantum yields were measured using an Edinburgh FLS-1000 spectrophotometer equipped with a 450 W xenon lamp as the light source. Fluorescence decay curves were recorded using the same spectrophotometer but using a picosecond pulsed diode (EPLED-320 nm, maximum pulse width = 950 ps). First, the IQY values were calculated according to the equation: $\mathrm{IQE} = \frac{\int L_S}{\int E_R - \int E_S}$. L_S represents the corresponding emission spectrum of the target phosphor. E_S and E_R are the spectra of the excitation light when the target phosphor is in the integrating sphere or not, respectively. Second, the absorption efficiency (AE) was calculated using the equation: $\mathrm{AE} = \frac{\int E_R - \int E_S}{\int E_R}$. Finally, the external quantum efficiency (EQE) is the product of these two. *In situ* high-pressure PL spectra were recorded using a home-designed spectrometer (Ideaoptics, Shanghai, China), and the 375 nm laser source was generated from the PicoQuant LDH diode head. The high pressure was generated by a symmetric diamond anvil cell (DAC) with type II diamonds polished to a diameter of 500 μm. Steel gaskets were pre-indented to ~40 μm thickness, and then 250 μm holes were drilled as the sample chambers, where pre-compressed samples together with ruby balls were placed. Silicone oil was employed as the pressure medium for all the high-pressure measurements, and the pressure was calibrated according to the fluorescence peak at 694.2 nm of the ruby balls, stimulated by the 405 nm incident light. Raman experiments were carried out using a Renishaw micro-Raman spectroscopy system (inVia Reflex) with a 532 nm laser line from a Nd:YAG laser source.

Results and discussion

Phase identification of LCYB: xCe^{3+} and LCYB: 0.01Ce^{3+}, yTb^{3+}

The standard PXRD pattern can be calculated according to the crystal structure of $LiCaY_5(BO_3)_3$ (CCDC 2056153).[26] The as-prepared phosphors (LCYB: xCe^{3+} and LCYB: 0.01Ce^{3+}, yTb^{3+}) were all characterized by PXRD at first and the patterns were aligned vertically, as shown in Fig. 1a and c. All patterns are identical by careful comparison, and importantly, an obvious left-shift can be observed as indicated by the representative peak at around 33°/2θ, which is assigned as the 116 reflection (see the right side of Fig. 1a and c). More accurately, the unit cell parameters can be extracted by Le Bail refinements on all

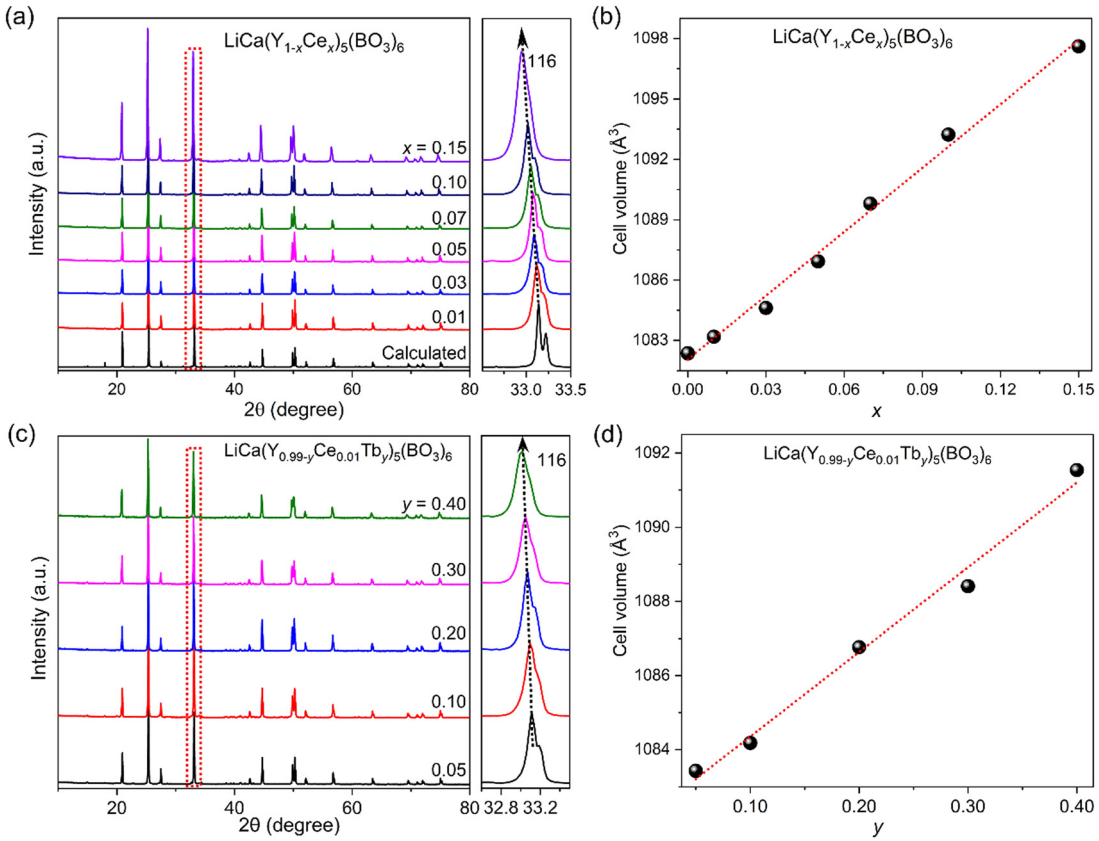

Fig. 1 PXRD patterns for (a) $LiCa(Y_{1-x}Ce_x)_5(BO_3)_6$ ($0.01 \le x \le 0.15$) and (c) $LiCa(Y_{0.99-y}Ce_{0.01}Tb_y)_5(BO_3)_6$ ($0.05 \le y \le 0.40$). The calculated pattern for $LiCaY_5(BO_3)_6$ is shown at the bottom, and the zero-shift for all data was pre-calculated and subtracted; (b) and (d) unit cell volume obtained from the Le Bail fitting against the doping contents.

data in the space group $P6_522$ (see Table S1 in ESI†). Exactly, the unit cell volume exhibits an almost linear expansion for both solid solutions (see Fig. 1b and d), confirming the successful cationic substitutions. In detail, the Shannon effective ionic radii for Y^{3+}, Ce^{3+}, and Tb^{3+} are 0.90, 1.01, and 0.923 Å in the six-fold coordination, respectively. The expansion rates are 102 Å^3/x, and 23 Å^3/y, respectively. It is close to the ratio between the radii differences, which is (1.01–0.90)/(0.923–0.90) = 4.78. The phase purity is the prerequisite for material characterizations; here the careful PXRD study ensures the following property investigation.

Photoluminescence properties of LCYB: xCe^{3+} and LCYB: 0.01Ce^{3+}, yTb^{3+}

PL excitation spectra for LCYB: xCe^{3+} display four major bands and cover the range from 220 to 380 nm (see Fig. 2a), which matches the low-cost UV or NUV LED chips. Upon the strongest excitation at ~336 nm, these phosphors all show the blue emission with a broad and asymmetric band ranging from 350 to 550 nm (see Fig. 2b). Note that the IQY is 51% for $LiCa(Y_{0.99}Ce_{0.01})_5(BO_3)_6$. In addition, an apparent red-shift of the maximal emission wavelength as well as the decline in intensity can be visualized. Such a red-shift for Ce^{3+} is frequently seen, such as in the cases of $BaLu_2Si_3O_{10}$: xCe^{3+},[11] $Ca_{0.75-1.5z}Li_{0.15}Al_{0.75}Si_{1.25}N_{2.9}O_{0.1}$: zCe^{3+},[27] $Ca_{1-2x}Ce_xLi_xAlSiN_3$,[28] $LiY_9(SiO_4)_6O_2$:Ce^{3+},[29] $NaSrY(BO_3)_2$:Ce^{3+},[30] and $CaY_2HfGa(AlO_4)_3$: Ce^{3+}.[7] There is also Ce^{3+}-to-Y^{3+} replacement in the latter three cases. In the literature, this red-shift was usually explained using the following equation: $D_q = \frac{1}{6}Ze^2\frac{r^4}{R^5}$, where Z is the anion charge, e is the electron charge, r is the radius of the d wave function, and R is the bond length between the central cation and its ligands.[31] Here, the parameter D_q represents the strength of the crystal-field splitting (CFS), which is only proportional to $1/R^5$. Therefore, the bond length is quite important to evaluate the CFS. According to the so-observed decreased energy difference between the lowest 5d-state and the ground state for Ce^{3+} (the red-shift), the D_q value should increase in magnitude and this means the Ce^{3+}–O^{2-} bond distance (R) should be shortened. Looking into the case of $LiCa(Y_{1-x}Ce_x)_5(BO_3)_6$ ($0.01 \le x \le 0.15$), the increase in Ce^{3+} concentration indeed leads to the expansion of the unit cell (see Fig. 1b), with a simultaneous increase in the Y/Ce–O bond distance definitely. It is known that the PL property depends on the local structural environment around the activators, so only the Ce^{3+}–O^{2-} bond matters, not the average Y/Ce–O bond distance. However, XRD just reflects the average structure, not the local structure. In other words, the increase in the average Y/Ce–O bond distance does not mean the expansion of

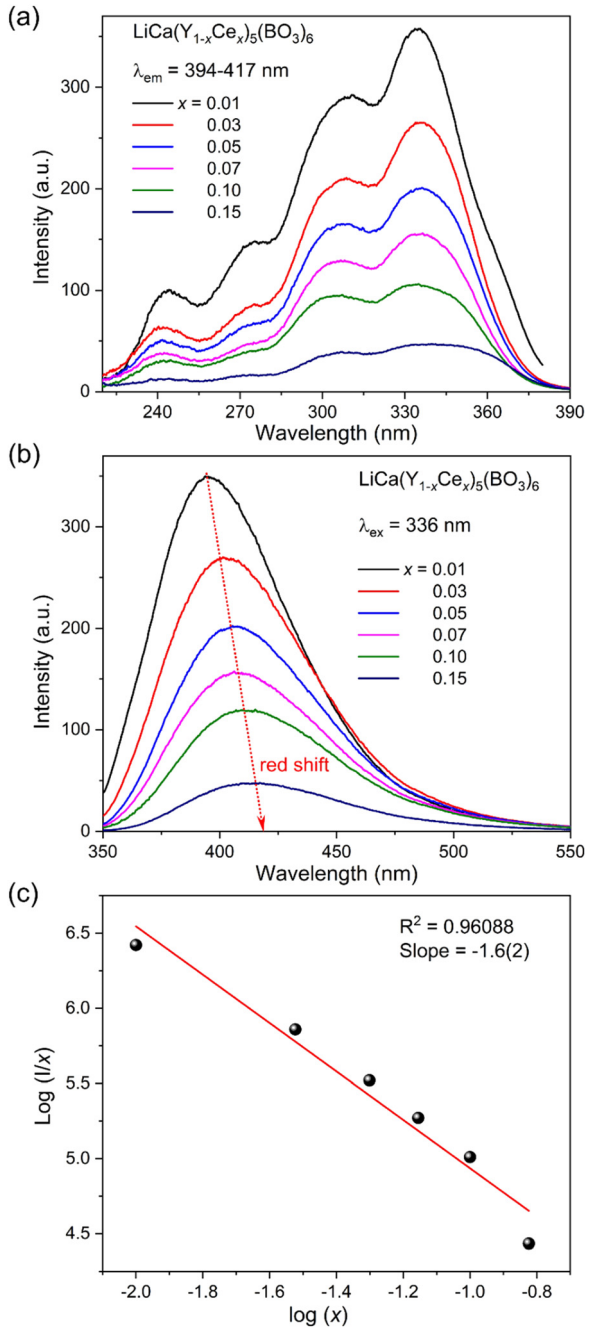

Fig. 2 (a) PL excitation and (b) emission spectra of $LiCa(Y_{1-x}Ce_x)_5(BO_3)_6$ ($0.01 \leq x \leq 0.15$) and (c) fitting curve according to the Dexter theory.

the Ce^{3+} polyhedra. When doping Ce^{3+} into $LiCaY_5(BO_3)_6$, Ce^{3+} locates in a smaller cavity and should suffer the compression, and when more Ce^{3+} was doped, such a compression becomes severer and the average Ce^{3+}–O^{2-} distance (the real R) should decrease, thus meaning the increase in D_q (CFS). People may say that the unit cell is also expanding. The problem is that such a unit cell expansion is a passive response to the Ce^{3+}-to-Y^{3+} substitution, which cannot fully satisfy the spatial requirement for the increasing contents of larger Ce^{3+}. Therefore, from the aspect of either the local structure or experimental observations, the red-shift phenomenon can be well explained.

The decline in emission intensity is due to the concentration quenching effect. Since this is a diluted system with low Ce^{3+} concentrations, it cannot be due to the exchange interactions but the electric multipolar interactions. The mechanism is usually analyzed according to the Dexter theory: $\log\left(\frac{I}{x}\right) = \log k + \left(\frac{\theta}{3}\right)\log(1+\beta(x))$, where I and x represent the emission intensity and the concentration of Ce^{3+}, and k and β specifically represent the interaction constants. The so-obtained values of θ, which could be 6, 8, or 10, represent the electric dipole-dipole, dipole-quadrupole, or quadrupole-quadrupole interactions, respectively.[11,32] Here, the linear fitting curve of log (I/x) to log (x) is plotted in Fig. 2c. The slope $(-\theta/3)$ was found to be $-1.6(2)$, and the value of θ is close to 6. The mechanism of energy transfer is near to dipole-dipole interactions, but the possibility of a partial exchange mechanism may remain.

As mentioned, it is ideal to combine Ce^{3+} with Tb^{3+} in LYCB to achieve a very high efficiency. For such an energy transfer, there needs to be an overlap between the PL emission of Ce^{3+} and the PL excitation of Tb^{3+}. As expected, this prerequisite is fulfilled by comparing the spectra for two singly doped phosphors, as shown in Fig. S1 (ESI†). Therefore, a series of co-doped phosphors LCYB: $0.01Ce^{3+}$, yTb^{3+} were rationally prepared. The PL excitation spectra by monitoring the Ce^{3+} emission at 387–393 nm are similar to that of the Ce^{3+} singly doped one (see Fig. 3a). When monitoring the emission at 543 nm (Tb^{3+} $^5D_4 \rightarrow {}^7F_5$ transition),[13] the PL excitation spectra contain the excitation for both Tb^{3+} and Ce^{3+} ions (see Fig. 3b), indicating the energy transfer from Ce^{3+}-to-Tb^{3+} in LCYB.[16,21]

In the following, these phosphors were excited by the Ce^{3+} 4f-5d transition at 336 nm, and the PL emission spectra (as shown in Fig. 4a) exhibit the blue emission band in the range of 350–475 nm (typical for Ce^{3+}) and sharp emission peaks ~489, 543, 590 and 624 nm, which correspond to the $^5D_4 \rightarrow {}^7F_6$, $^5D_4 \rightarrow {}^7F_5$, $^5D_4 \rightarrow {}^7F_4$ and $^5D_4 \rightarrow {}^7F_3$ transitions for Tb^{3+} ions, respectively.[16,19] The variations for Ce^{3+} and Tb^{3+} emissions are different due to the energy transfer, and the Tb^{3+} emission reaches the maximum at $y = 0.2$. Note that the IQY increases from 51% at $y = 0$ to 89% at $y = 0.20$, and it decreases to 60% at $y = 0.3$ (see Table S2, ESI†). Considering that the absorption efficiencies for $LiCa(Y_{0.99}Ce_{0.01})_5(BO_3)_6$ and $LiCa(Y_{0.79}Ce_{0.01}Tb_{0.2})_5(BO_3)_6$ are 67% and 59% (see Fig. S2, ESI†), respectively, the calculated EQE value increases indeed from 34% for the Ce^{3+} singly doped phosphor to the maximal value of 53% by co-doping 20% Tb^{3+}. Accordingly, this strategy for co-doping Tb^{3+} in LYCB is successful to increase the overall IQY.

To further confirm the Ce^{3+}-to-Tb^{3+} energy transfer, the fluorescence decay curves of Ce^{3+} for LCYB: $0.01Ce^{3+}$, yTb^{3+} are presented in Fig. 4b ($\lambda_{ex} = 320$ nm, $\lambda_{em} = 393$ nm), and then the decay curves could be fitted by the double-exponential function:[33] $I(t) = I_0 + A_1\exp\left(\frac{-t}{\tau_1}\right) + A_2\exp\left(\frac{-t}{\tau_2}\right)$. All decay

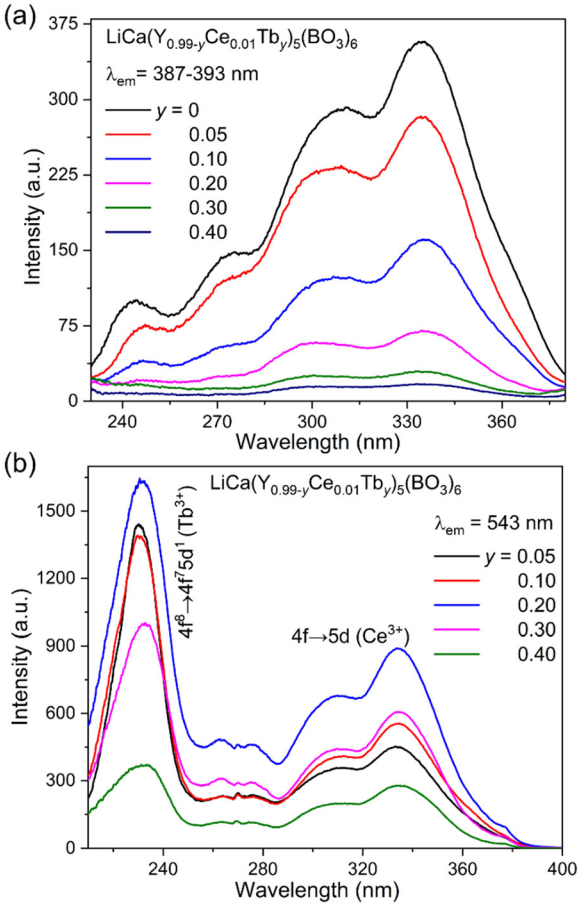

Fig. 3 PL excitation spectra by monitoring (a) the Ce^{3+} emission at λ_{em} = 387–393 nm and (b) the Tb^{3+} emission at λ_{em} = 543 nm.

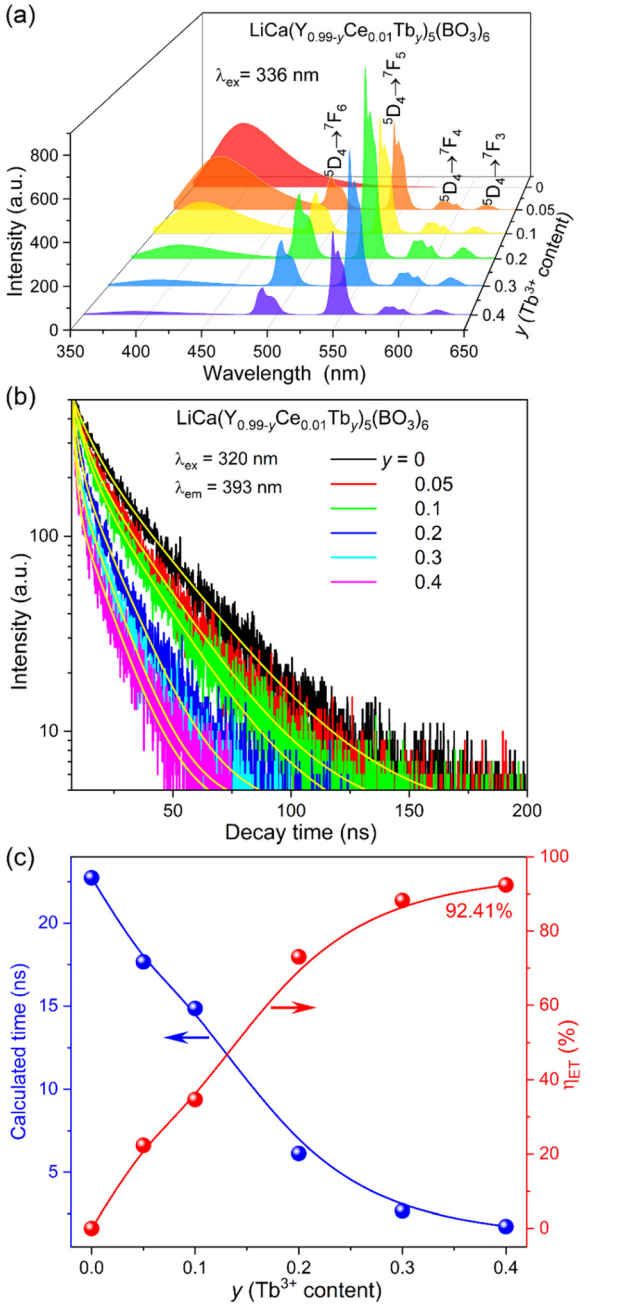

Fig. 4 (a) PL emission spectra of $LiCa(Y_{0.99-y}Ce_{0.01}Tb_y)_5(BO_3)_6$ ($0 \le y \le 0.40$) under the excitation of λ_{ex} = 336 nm, (b) fluorescence decay curves for Ce^{3+} emission; and (c) calculated lifetime and the Ce^{3+}-to-Tb^{3+}energy transfer efficiency against y.

curves could be fitted very well, where t and I are the time (ns) and luminescence intensity, respectively. As shown in Table S3 (ESI†), A_1 and A_2 are constants, and τ_1 and τ_2 are the short and long-decay components, respectively. The value of the average lifetime τ can be obtained utilizing the expression:[16] $\tau = \frac{A_1\tau_1^2 + A_2\tau_2^2}{A_1\tau_1 + A_2\tau_2}$. Fig. 4c shows the plots of the average lifetime of Ce^{3+}, which decreases from 22.74 to 1.73 ns. It firmly proves the Ce^{3+}-to-Tb^{3+} energy transfer in LCYB:0.01Ce^{3+}, yTb^{3+} phosphors. Generally, the energy transfer efficiency (η_{ET}) from Ce^{3+}-to-Tb^{3+} can be approximately calculated utilizing the lifetime variations of Ce^{3+} by the equation:[15,16] $\eta_{ET} = 1 - \frac{\tau}{\tau_0}$, where τ_0 and τ represent the corresponding luminescence lifetimes of sensitizer Ce^{3+} ions in the absence and presence of activator ions, respectively. In Fig. 4c, a monotonously increasing tendency is observed and it finally achieves 92.41% at y = 0.40.

Similar to the case of Ce^{3+}-concentration quenching, the Ce^{3+}-to-Tb^{3+} should occur *via* electronic multipolar interactions. The Inokuti–Hirayama (I–H) model has been employed to evaluate the mechanism:[15,34] $I(t) = I_0(t)\exp\left[-\frac{4}{3}\pi\Gamma\left(1-\frac{3}{S}\right)n_A\alpha^{3/S}t^{3/S}\right]$, where $I_0(t)$ characterizes the decay function of donors without the acceptors, n_A is the number of acceptor ions per unit volume, α is the rata constant for energy transfer, and S = 6, 8 and 10 are the coefficients for dipole–dipole, dipole–quadrupole, and quadrupole–quadrupole interaction, respectively. In order to obtain S, the I–H model equation was transformed into $\log\left[-\mathrm{Ln}\left(\frac{I(t)}{I_0(t)}\right)\right] = \frac{3}{S}\log(t) + \log\left[\frac{4}{3}\pi\Gamma\left(1-\frac{3}{S}\right)n_A\alpha^{3/S}\right]$. It can be found that $\log\left[-\mathrm{Ln}\left(\frac{I(t)}{I_0(t)}\right)\right]$ acts as a linear function of

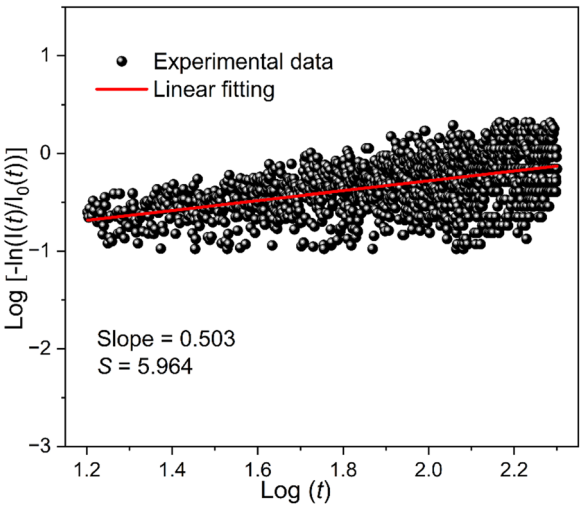

Fig. 5 Inokuti–Hirayama model fitting for the data of $LiCa(Y_{0.94}Ce_{0.01}Tb_{0.05})_5(BO_3)_6$.

$\log(t)$ with a slope of $3/S$. In order to better understand the Ce^{3+}-to-Tb^{3+} energy transfer mechanism, we plotted the $\log\left[-\mathrm{Ln}\left(\frac{I(t)}{I_0(t)}\right)\right]$ *versus* $\log(t)$ of Ce^{3+} in the LCYB:0.01Ce^{3+}, 0.05Tb^{3+} phosphor, as shown in Fig. 5. The slope of the fitting line is approximately 0.503; therefore, the calculated value of S is close to 6, indicating that energy transfer from Ce^{3+}-to-Tb^{3+} occurs *via* the electric dipole–dipole interaction.

The Commission International de L'Eclairage (CIE) was employed to evaluate the chromaticity coordinates of phosphors through their emission spectra. It changes from (0.157, 0.045) to (0.297, 0.548) when increasing y (see Fig. 6a). The emission color changes from blue to green as also directly indicated by the photographs of the phosphors under a 310 nm UV lamp (see the insets in Fig. 6a). To further evaluate the potential as LED-pumped phosphors, two representative phosphors with Ce^{3+}-doping and Ce^{3+}/Tb^{3+} co-doping are combined with 310 nm LED chip with an operating voltage of 3 V. As shown in Fig. 6b and 6c, both can be efficiently pumped by the working UV-LED chip and display characteristic emissions. Since the working condition of the LED chip is hot, the *in situ* high-temperature PL spectra under the excitation of 336 nm were recorded for LCYB:0.01Ce^{3+}, 0.2Tb^{3+}, and are shown in Fig. 7. The integral emission intensity as a function of the temperature is provided in the inset, and it exhibits a typical decreasing tendency due to the temperature quenching effect. The calculated CIE coordinates based on the spectra are displayed in Fig. S3 (ESI†), which changes slightly when heating up. At 423 K, it remains 58% of that at room temperature, indicating the sufficient thermal stability as LED-pumped phosphors.

In situ high-pressure photoluminescence of LYCB:0.01Ce^{3+}

In situ PL spectra were recorded for LYCB:0.01Ce^{3+} at high pressures from 0.5 to 20.1 GPa, where the incident light was generated by the laser with the fixed wavelength at 375 nm. The original spectra are displayed in Fig. 8a, and the emission spectra exhibit the variations in both intensity and position. For the former one, the constant wavelength at 375 nm is not the optimal wavelength, which is supposed to be 336 nm; therefore, the first increase in intensity is likely due to the red-shift (*i.e.* from 336 nm to longer wavelengths) of the Ce^{3+} excitation band induced by the external high pressure.

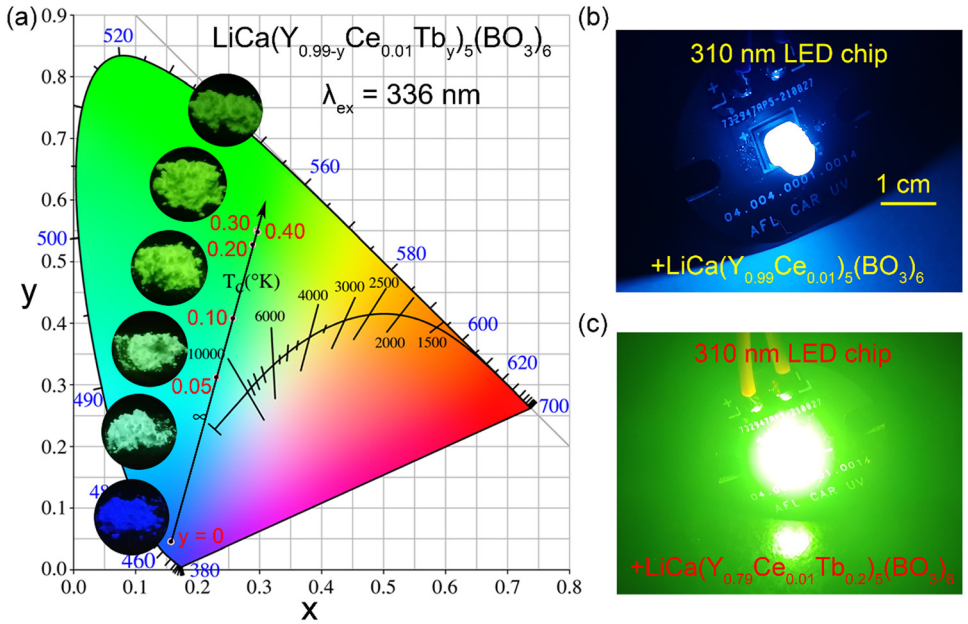

Fig. 6 (a) CIE diagram for $LiCa(Y_{0.99-y}Ce_{0.01}Tb_y)_5(BO_3)_6$ ($0 \le y \le 0.40$) phosphors under 336 nm excitation. Insets show the digital photographs of the phosphors with different Tb^{3+} concentrations under a 310 nm UV lamp. Photographs of the 310 nm LED chip combined with (b) $LiCa(Y_{0.99}Ce_{0.01})_5(BO_3)_6$ and (c) $LiCa(Y_{0.79}Ce_{0.01}Tb_{0.2})_5(BO_3)_6$.

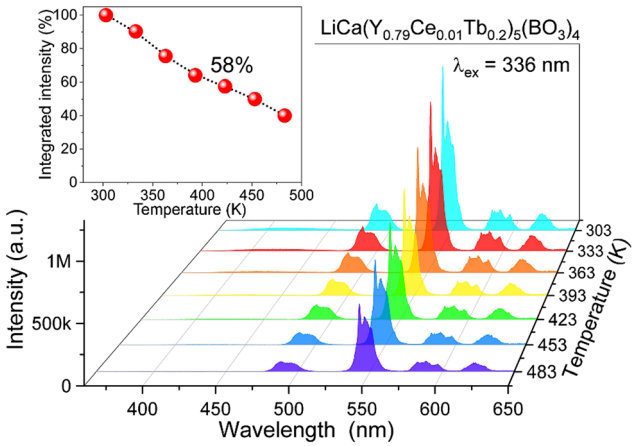

Fig. 7 *In situ* high-temperature PL emission spectra for $LiCa(Y_{0.79}Ce_{0.01}Tb_{0.2})_5(BO_3)_6$ under the excitation at 336 nm. Normalized emission intensity along with the temperature is plotted as the inset.

At extremely high pressures (>7 GPa), there seems to be a pressure-quenching effect, leading to a decrease in the emission intensity. In the following, we present the normalized PL spectra of LYCB:0.01Ce^{3+} in Fig. 8b. An obvious and monotonous red-shift in wavelength can be observed for the emission band, which indicates the decrease in the energy difference between 5d and 4f states of Ce^{3+}. This is consistent with the likely red-shift of the excitation band. By physical compression, the average Ce–O bonds become shorter and the CFS (D_q) will be significantly enhanced,[35,36] and the corresponding excitation and emission spectra are both supposed to exhibit an overall red-shift.

As shown in 9a, the wavelength at the maximal intensity (λ_{max}) exhibits a 43 nm red-shift from 0.5 to 20.1 GPa, and interestingly, this is quite linear. A simple linear fitting was applied and the calculated pressure-dependent susceptibility $d\lambda_{max}/dP$ is 2.05 nm/GPa, which is even much higher than that for the ruby sensor (*i.e.*, Al_2O_3:Cr^{3+}, 0.36 nm/GPa).[24] As interpreted above, the red-shift in emission bands is due to the decreased difference in energy; therefore, it can also be depicted using the changes in wavenumbers and energy quantitatively. As shown in Fig. 9b, both exhibit a linear behavior with the fitting equations $\delta_{max} = 23009.66 - 99.28 \times P$ and $E_{max} = 2.8532 - 0.0123 \times P$, where the pressure-dependent susceptibility are 99.28 cm^{-1}/GPa and 0.0123 eV/GPa, respectively. In addition to the red-shift, the full width at half maximum (FWHM) of the Ce^{3+} emission band also exhibits a close-to-linear relationship, increasing below 15 GPa, as shown in Fig. S4 (ESI†). It finally reaches 138.7 nm at 20.1 GPa. The FWHM is related to structure rigidity and symmetry, phonon energy, the Huang-Rhys coupling factor, *etc.*[37] Under the high pressure, the local coordination symmetry of Ce^{3+} tends to be more distorted, thus the increase in FWHM is understandable.

Fig. 10 shows the evolution of the CIE chromaticity coordinate by increasing the external pressure, where the emission color changes from deep-blue (0.195, 0.124) to blue-green (0.255, 0.305). Detailed calculated CIE coordinates are provided in Table S4 (ESI†). An *in situ* high-pressure Raman spectra experiment was also conducted to confirm the structure stability under extreme conditions. As shown in Fig. 11, the vibrational bands centered at ~210 and 355 cm^{-1} are likely due to the metal-oxygen vibrations, and translational and vibrational motions of BO_3. Five peaks at 500, 646, 690, 712 and 789 cm^{-1} could be assigned to bending vibration modes of BO_3. The weak peak around 938 cm^{-1} was attributed to the symmetric stretching vibrations of BO_3.[38,39] When increasing the pressure, other than the normal peak shifting and broadening, there was no additional Raman peak, and the whole pattern was recovered after the pressure release, all of which indicate that no phase transition occurs. In fact, the PL spectrum by releasing the high pressure also overlaps with the original one (see Fig. 8), which consolidates the stability of the phosphor.

Ruby balls are commonly used as the pressure sensor in DAC experiments, here LCYB:0.01Ce^{3+} may also have the potential to be a visual pressure sensor in other application scenarios. Although it does not possess sharp peaks like those for Al_2O_3:Cr^{3+}, its high quantum efficiency, pressure-dependent susceptibility, sensitivity in CIE chromaticity coordinate, and

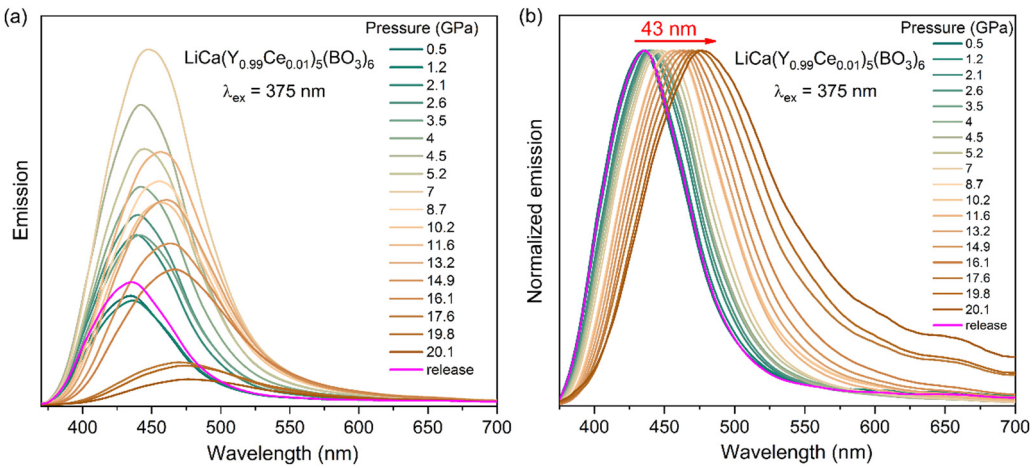

Fig. 8 (a) Original and (b) normalized emission spectra of $LiCa(Y_{0.99}Ce_{0.01})_5(BO_3)_6$ at different pressures (λ_{ex} = 375 nm).

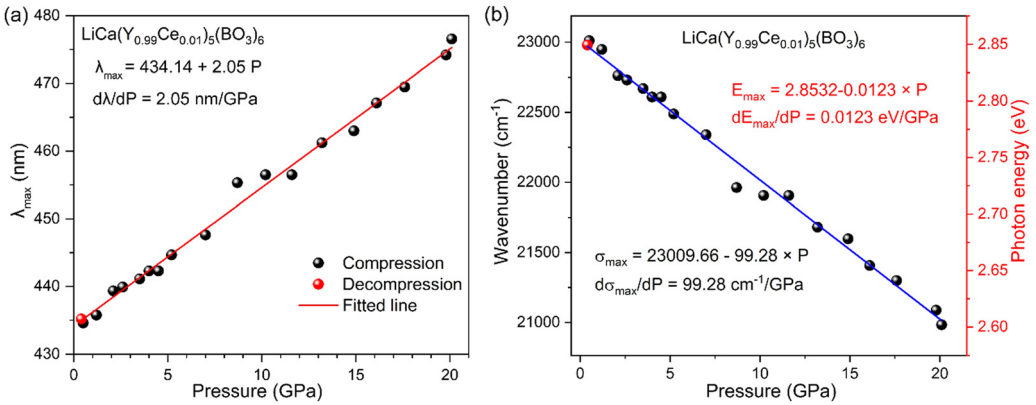

Fig. 9 Band centroid in the form of (a) wavelength or (b) wavenumber/photon energy for the Ce^{3+} emission band as a function of pressure.

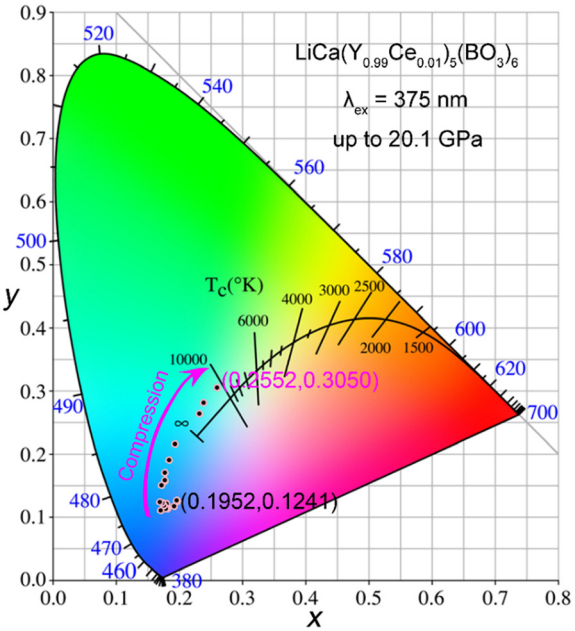

Fig. 10 CIE coordinates of the samples at different pressures from 0.5 GPa to 20.1 GPa.

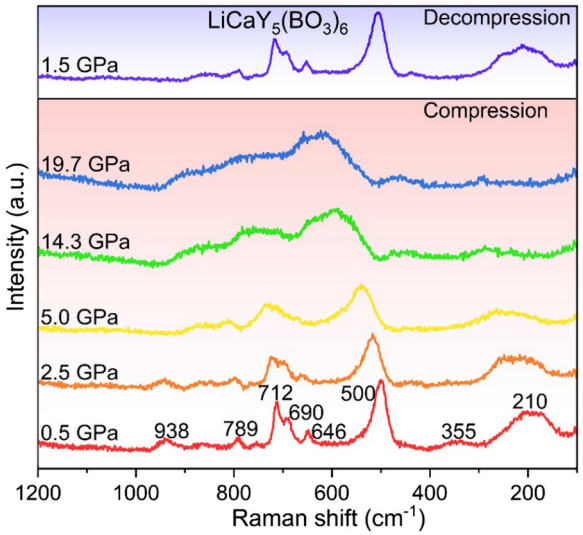

Fig. 11 *In situ* high-pressure Raman spectra of $LiCaY_5(BO_3)_6$.

stability are really advantageous. Comparing to two recently reported Ce^{3+}-phosphors, which are considered as possible visual pressure sensors due to their broad emission band, LCYB:0.01Ce^{3+} has a higher pressure sensitivity and a better linearity than $Mg_2Gd_8(SiO_4)_6O_2:Ce^{3+}$ ($d\lambda_{max}/dP$ = 1.85 nm/GPa);[36] it has a wider applicable pressure region and a higher quantum efficiency than $Ca_2Gd_8Si_6O_{26}:Ce^{3+}$ (<10 GPa).[35]

Conclusion

The PXRD patterns of $LiCa(Y_{1-x}Ce_x)_5(BO_3)_6$ ($0.01 \leq x \leq 0.15$) and $LiCa(Y_{0.99-y}Ce_{0.01}Tb_y)_5(BO_3)_6$ ($0.05 \leq y \leq 0.4$) exhibit no impurity peaks and the accurate cell volumes obtained from Le Bail fitting exhibit the typical linear expansion, indicating the successful cationic substitutions. Ce^{3+} exhibits typical broad excitation bands from 220 to 380 nm, and a strong blue emission band. The optimal IQY is 51% at x = 0.01. When another activator Tb^{3+} was introduced, the IQY can be enhanced significantly to 89% in $LiCa(Y_{0.79}Ce_{0.01}Tb_{0.2})_5(BO_3)_6$ due to the fast and efficient Ce^{3+}-to-Tb^{3+} energy transfer, which is likely through the dipole-diploe electric interaction. Color tunable emissions from blue to green can be obtained by increasing the Tb^{3+} content, and a preliminary test using a 310 nm LED chip coupled with $LiCa(Y_{0.99}Ce_{0.01})_5(BO_3)_6$ and $LiCa(Y_{0.79}Ce_{0.01}Tb_{0.2})_5(BO_3)_6$ leads to blue and green emissions as expected. The sufficient thermal stability was also proved by *in situ* high-temperature PL spectra. When applying high pressures to LCYB:0.01Ce^{3+}, the structure maintains up to 20.1 GPa. It exhibits an almost linear red-shift of the wavelength at the maximal emission, and most importantly, this pressure-dependent susceptibility $d\lambda_{max}/dP$ is as high as 2.05 nm/GPa, making it a promising candidate for optical pressure sensors.

Author contributions

Yan Gao: writing – original draft, investigation. Yunwei Zhao: investigation. Pengfei Jiang: investigation. Ting Wen: investigation. Yonggang Wang: writing – review & editing. Rihong Cong: writing – review & editing, supervision. Tao Yang: writing – review & editing, project administration.

Conflicts of interest

The authors declare no competing financial interest.

Acknowledgements

This work was financially supported by the National Natural Science Foundation of China (22171031, 22171032, 22271030) and Natural Science Foundation of Chongqing (cstc2021ycjh-bgzxm0089).

References

1 R. Shi, X. J. Zhang, Z. X. Qiu, J. L. Zhang, S. Z. Liao, W. L. Zhou, X. H. Xu, L. P. Yu and S. X. Lian, *Inorg. Chem.*, 2021, **60**, 19393–19401.
2 S. S. Ye, J. Y. Ding and Q. S. Wu, *Chem. Eng. J.*, 2022, **428**, 131238.
3 D. Zhang, X. T. Zhang, B. F. Zheng, Q. Sun, Z. B. Zheng, Z. Shi, Y. H. Song and H. F. Zou, *Adv. Opt. Mater.*, 2021, **9**, 2100337.
4 B. Yu, Y. C. Li, Y. J. Wang and L. Geng, *J. Alloys Compd.*, 2021, **874**, 159862.
5 J. W. Qiao, L. X. Ning, M. S. Molokeev, Y. C. Chuang, Q. L. Liu and Z. G. Xia, *J. Am. Chem. Soc.*, 2018, **140**, 9730–9736.
6 P. P. Dang, D. J. Liu, G. G. Li, A. A. Al Kheraif and J. Lin, *Adv. Opt. Mater.*, 2020, **8**, 1901993.
7 J. M. Chan, L. N. Cao, W. Li, N. Ma, Z. Xu and X. Y. Huang, *Inorg. Chem.*, 2022, **61**, 6953–6963.
8 Y. Q. Li, N. Hirosaki, R. J. Xie, T. Takeda and M. Mitomo, *Chem. Mater.*, 2008, **20**, 6704–6714.
9 C. Y. Wang, O. M. ten Kate, T. Takeda and N. Hirosaki, *J. Mater. Chem. C*, 2017, **5**, 8295–8300.
10 X. Y. Fan, X. Y. Sun, C. M. Liu, W. L. Tian, M. Li, Y. S. Luo and C. L. Wu, *J. Lumin.*, 2022, **242**, 118594.
11 K. Li, S. S. Liang, H. Z. Lian, M. M. Shang, B. G. Xing and J. Lin, *J. Mater. Chem. C*, 2016, **4**, 3443–3453.
12 Y. Xiao, Z. D. Hao, L. L. Zhang, W. G. Xiao, D. Wu, X. Zhang, G. H. Pan, Y. S. Luo and J. H. Zhang, *Inorg. Chem.*, 2017, **56**, 4539–4545.
13 D. Wu, Y. Xiao, L. L. Zhang, X. T. Dong, S. F. Zhao, W. P. Zhou, Q. S. Lu and J. H. Zhang, *J. Mater. Chem. C*, 2020, **8**, 17176–17184.
14 G. Li, Y. H. Wang, W. Zeng, W. B. Chen, S. C. Han, H. J. Guo and Y. Y. Li, *J. Mater. Chem. C*, 2016, **4**, 3304–3312.
15 J. Y. Li, X. F. Zhou, J. Y. Ding, X. P. Zhou and Y. H. Wang, *J. Mater. Chem. C*, 2019, **7**, 2257–2266.
16 H. Chen and Y. H. Wang, *Inorg. Chem.*, 2019, **58**, 7440–7452.
17 H. R. Li, Y. J. Liang, S. Q. Liu, W. L. Zhang, Y. Y. Bi, Y. M. Gong, Y. J. Chen and W. Lei, *J. Mater. Chem. C*, 2021, **9**, 2569–2581.
18 S. Y. Wang, B. Devakumar, Q. Sun, J. Liang, L. L. Sun and X. Y. Huang, *J. Lumin.*, 2020, **220**, 117012.
19 Q. Dong, J. J. Yang, J. Cui, F. F. Xu, F. L. Yang, J. Q. Peng, F. Du, X. Y. Ye and S. H. Yang, *Dalton Trans.*, 2020, **49**, 1935–1946.
20 L. L. Sun, J. Liang, S. Y. Wang, Q. Sun, B. Devakumar and X. Y. Huang, *Mater. Today Energy*, 2020, **17**, 100487.
21 X. Y. Huang, J. Liang, S. Rtimi, B. Devakumar and Z. J. Zhang, *Chem. Eng. J.*, 2021, **405**, 126950.
22 L. P. Dong, L. Zhang, Y. C. Jia, B. Q. Shao, W. Lü, S. Zhao and H. P. You, *CrystEngComm*, 2019, **21**, 6226–6237.
23 J. L. Pan, Z. Y. Guo, Z. P. Zhu, Z. S. Sun, T. T. Zhang, J. L. Zhang and X. G. Zhang, *Ceram. Int.*, 2018, **44**, 20732–20738.
24 J. D. Barnett, S. Block and G. J. Piermarini, *Rev. Sci. Instrum.*, 1973, **44**, 1–9.
25 *TOPAS, V4.1-beta*, Bruker AXS, Karlsruhe, Germany, 2004.
26 Y. Gao, C. Yin, P. F. Jiang, W. L. Gao, R. H. Cong and T. Yang, *J. Solid State Chem.*, 2021, **293**, 121821.
27 S. H. You, S. X. Li, L. Wang, T. Takeda, N. Hirosaki and R. J. Xie, *Chem. Eng. J.*, 2021, **404**, 126575.
28 Y. Q. Li, N. Hirosaki, R. J. Xie, T. Takeda and M. Mitomo, *Chem. Mater.*, 2008, **20**, 6704–6714.
29 W. J. Zhou, F. J. Pan, L. Zhou, D. J. Hou, Y. Huang, Y. Tao and H. B. Liang, *Inorg. Chem.*, 2016, **55**, 10415–10424.
30 X. G. Zhang, X. Chen, C. Zhou, J. Q. Fan, W. Y. Zhou, Q. Pang, L. Y. Zhou and Y. R. Hu, *J. Lumin.*, 2022, **251**, 119278.
31 G. G. Li, Y. Tian, Y. Zhao and J. Lin, *Chem. Soc. Rev.*, 2015, **44**, 8688–8713.
32 S. Wu, P. X. Xiong, X. Q. Liu, Y. B. Fu, Q. Liu, Y. Chao, Q. Dong, Y. Y. Li, W. W. Chen, Y. Chen, Z. J. Ma and M. Y. Peng, *J. Mater. Chem. C*, 2021, **9**, 3672–3681.
33 P. P. Dang, S. S. Liang, G. G. Li, Y. Wei, Z. Y. Cheng, H. Z. Lian, M. M. Shang, A. A. Al Kheraif and J. Lin, *Inorg. Chem.*, 2018, **57**, 9251–9259.
34 M. M. Jiao, Q. F. Xu, M. L. Liu, C. L. Yang and Y. J. Yu, *Phys. Chem. Chem. Phys.*, 2018, **20**, 26995–27002.
35 T. Zheng, L. H. Luo, P. Du, S. Lis, U. R. Rodríguez-Mendoza, V. Lavín, I. R. Martín and M. Runowski, *Chem. Eng. J.*, 2022, **443**, 136414.
36 B. F. Zheng, X. T. Zhang, D. Zhang, F. K. Wang, Z. B. Zheng, X. Y. Yang, Q. Yang, Y. H. Song, B. Zou and H. F. Zou, *Chem. Eng. J.*, 2022, **427**, 131897.
37 Y. C. Wang, T. Seto, K. Ishigaki, Y. Uwatoko, G. J. Xiao, B. Zou, G. S. Li, Z. B. Tang, Z. B. Li and Y. H. Wang, *Adv. Funct. Mater.*, 2020, **30**, 2001384.
38 X. B. Hu, J. Y. Wang, B. Teng, C.-K. Loong and M. Grimsditch, *J. Appl. Phys.*, 2005, **97**, 033501.
39 R. H. Cong, T. Yang, J. L. Sun, Y. X. Wang and J. H. Lin, *Inorg. Chem.*, 2013, **52**, 7460–7466.

